Satellite-Observed Characteristics of Winter Monsoon Cloud Clusters

MARK WILLIAMS* AND ROBERT A. HOUZE, JR.

Department of Atmospheric Sciences, University of Washington, Seattle, WA 98195

(Manuscript received 10 December 1985, in final form 26 August 1986)

ABSTRACT

An objective algorithm is devised which is capable of locating tropical cloud clusters at the point of initiation, tracking them to the point of dissipation and thereby accumulating statistics on their size distributions and preferred geographical locations and times of occurrence. The technique is able to account for periods of growth, mergers, splits and decay, which take place during the lifetime of an individual cluster. It is used to derive statistics on cloud clusters observed during the Winter Monsoon Experiment, which was conducted in the region of the "maritime continent," near Borneo, in December, 1978. The size distribution of the clusters identified and tracked shows that by far most of the cumulative cloud cover was accounted for by a few very large clusters. This result implies that the vertical distribution of diabatic heating in the region of the experiment was strongly influenced by dynamical and radiative processes in the widespread stratiform cloud and precipitation areas that typify very large clusters. A pronounced diurnal cycle was characterized by a preference for the very large clusters to reach the middle of their lifetime over the sea during morning. Monsoon "surge" conditions over the South China Sea also strongly favored the occurrence of large clusters over the water north of Borneo.

1. Introduction

Clouds in the tropics occur in a spectrum of sizes ranging from small isolated nonprecipitating cumulus to large "cloud clusters," which exhibit mesoscale organization and account for most of the rainfall. While all of these clouds affect the vertical distribution of heating in the troposphere, the cloud clusters are most significant since they are the seat of most of the total heating. Cloud clusters are characterized by widespread stratiform cloud decks, the tops of which are seen as cirrus shields in satellite pictures. These shields are typically 100–1000 km in dimension, and radar data show that beneath them the rainfall is contained within two types of structures: embedded deep convective cells and mesoscale regions of stratiform precipitation.

Houze (1982) showed that because of the contribution of stratiform processes cloud clusters are characterized by stronger heating at upper levels and weaker heating at lower levels than would be the case if deep convective cells were acting alone. Webster and Stephens (1980) pointed out that the radiative effects of the upper-level stratiform cloud deck results in upper tropospheric heating even after the precipitation has ceased. Hartmann et al. (1984) studied the effects of different heating profiles on a linear steady state global model and found that mature cloud-cluster heating profiles, which include stratiform cloud effects, result in simulated tropical east–west circulations that are in better agreement with observations than those which are produced by a more purely convective heating profile.

Since the magnitude and vertical distribution of heating imparted to the atmosphere by tropical cloud systems are largely determined by the presence or absence of large cloud clusters, it is evident that a global climatology of cloud-cluster occurrence would be useful for establishing the net effects of clusters on large-scale dynamics and climate. The objectives of this study are to develop a technique for obtaining such a climatology and to test the method on data from the Winter Monsoon Experiment (WMONEX), which was carried out near Borneo in December, 1978. In pursuit of these objectives, we have developed a method for automatically compiling and quantifying aspects of the behavior of tropical cloud clusters from digitally recorded infrared satellite imagery and used it on data from WMONEX. In this process, we have obtained a valuable cloud-cluster climatology for the WMONEX region as well as an analytical technique that will be useful in future work aimed at obtaining cloud-cluster climatologies for other regions and ultimately for the whole globe.

The technique we have developed uses a simple algorithm to identify and track individual cloud clusters. The method has similarities to previous work in which clusters have been tracked automatically (Woodley et al., 1980) and manually (Aspliden et al., 1976; Payne and McGarry, 1977; Martin and Schreiner, 1981), except that we do not terminate a cluster when it splits into two or more elements or merges with another

---

* Present affiliation: Bureau of Meteorology Research Center, Melbourne, Vic. 3001, Australia.

cluster. Since our method allows a cloud cluster to retain its identity even though it might undergo splits and mergers during its lifetime, the growth and decay processes of real cloud clusters are retained more accurately.

In the following sections of this paper, we first describe the data and explain the tracking algorithm. Then we present the results obtained from the application of the technique to the WMONEX data. Size distributions and variations of structure and behavior with time of day, monsoon intensity, and proximity to land and sea have been determined for all the cloud clusters in WMONEX. Each cluster, which reached a minimum threshold size, was traced from its starting time to end time with the following parameters being computed and recorded: start time, midtime, end time, maximum area, lifetime, amount of time over land or sea, movement, and number of splits and/or mergers. These parameters have been mapped and compiled statistically to convey a more comprehensive picture of cloud processes over the WMONEX region than has heretofore been available.

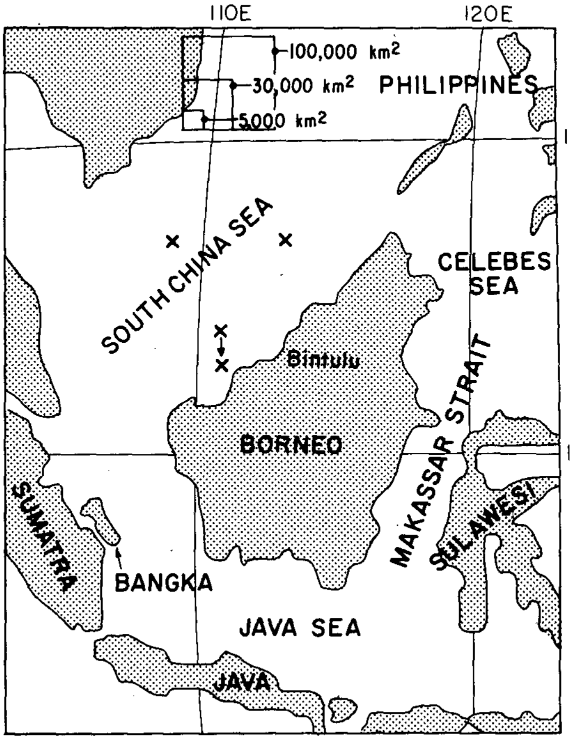

FIG. 1. Domain of analysis. This study identifies and tracks all cloud clusters that occurred in this region during WMONEX. Locations of Soviet research ships are indicated by ×'s. The southern ship changed locations during the experiment (arrow). Inset areas indicate sizes of clusters referred to in the text.

2. The data

The period of WMONEX selected for testing our analysis scheme was 9–29 December 1978. This period, also studied by Houze et al. (1981), Johnson and Priegnitz (1981) and Geotis and Houze (1985), was the time of most intensive data collection during the experiment.

The data used for this study were digital IR brightness values from the Japanese geostationary meteorological satellite GMS-1. They were supplied by the Space Science and Engineering Center, University of Wisconsin. The area covered was approximately 15°N to 10°S, 100° to 125°E (Fig. 1). The resolution of the IR imagery was approximately 2.4 km. The observation times were 0233, 0533, 0833, 1133, 1533, 1733, 2033 and 2333 UTC which corresponds to 0953, 1253, 1553, 1853, 2253, 0053, 0353 and 0653 local standard time (LST) at 110°E. Unless otherwise stated, all times in this paper will be given in local standard time at 110°E. Two pictures were missing from the sequence, the 1733 UTC pictures for 24 and 27 December 1978. Both of these pictures were available on microfilm supplied by the Japanese Meteorological Agency and inspection revealed that they were very similar to the previous pictures for 1533 UTC. In order to fill the two gaps left by the missing pictures, copies of the two previous pictures were substituted in place of the missing ones. This completed the set of 168 pictures.

3. Algorithm for identifying and tracking cloud clusters

The infrared satellite data are particularly convenient for identifying and tracking cloud clusters since they display prominently the cold cirrus shields, which account for most of the areal coverage and exist throughout the long lifetimes of clusters. Our technique searches through the spatial domain shown in Fig. 1 for all the contiguous areas of cloud top with equivalent blackbody temperature < 213 K at a given time. This temperature threshold is, of course, arbitrary but in WMONEX it appeared to be more closely related to areas covered by precipitation than did lower or higher thresholds.

a. Basic idea of the algorithm

Cloud areas that satisfy the temperature threshold criterion and exceed 5×10^3 km^2 in area are each tagged and called *cluster elements (or CEs)*. The satellite picture for a particular time is referred to as a *frame* and a CE is an individual cloud mass in a single frame. It is tagged with a number that is unique only in the frame in which it is located. A *cloud cluster* is defined as a sequence of CEs that can be tracked from one frame to the next. The cluster thus exists over a period of time that encompasses its lifetime, and at any one time during that period it may consist of one or more CEs. The technique for tracking a cluster from one time to the next simply assumes that CEs at a later time correspond to those at an earlier time if their positions overlap sufficiently. The basic requirement is

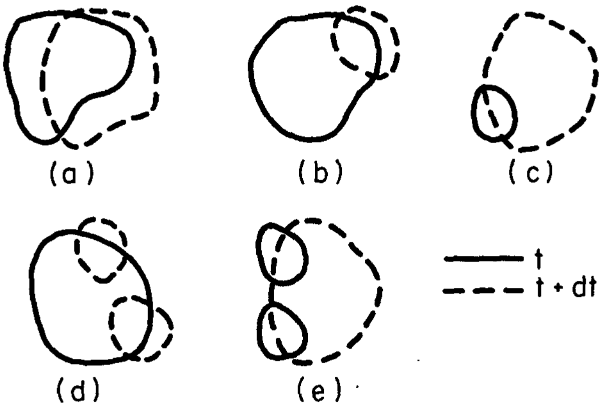

FIG. 2. Examples illustrating how the cloud-cluster tracking algorithm works. Five hypothetical cases are shown in which a cluster is tracked from time t to $t + dt$. See text for further explanation.

that the area covered by CEs in two successive frames must overlap by a specified amount going *either* forward *or* backward in time. A match is made if a CE in one frame covers at least 50% or 10^4 km^2 of the area of a CE in a second frame (either the one just earlier or the one just later). It is the either/or aspect of this overlap requirement that is most important. The hypothetical examples in Fig. 2 illustrate how the either/or aspect allows for growth and decay to be captured and for mergers and splits to be included in the life histories of clusters. Panel a illustrates an especially simple case in which a match is made by comparing both forward and backward in time. The match made in Fig. 2b, however, is made going forward only; that is, over half of the CE at the later time is overlapped by the CE at the earlier time. A match is not made going backward in time since the cluster is shrinking rapidly. However, since the match is made going forward in time, the cluster is properly traced through its dissipating stage. Figure 2c is an example of a rapidly growing cluster, which is tracked by satisfying the overlap requirement going backward but not forward in time. An example of how the tracking routine accounts for a split of a cluster is shown in Fig. 2d. At the earlier time, a cluster consists of a single large cluster element. At the later time, two smaller CEs are each overlapped, over more than half of their areas, by the earlier CE. Thus, the cluster is considered at the later time to consist of the *two* CEs. In this way, we continue to follow the history of the cluster even though it has split into more than one component CE. Note that the split is identified only by going forward in time since 50% of the CE at the earlier time is not overlapped by either of the later CEs. Figure 2e shows how a merger is identified by comparing backward in time.

Since some of the matches that must be made to trace the sequence of CEs comprising a cluster can only be made by comparing forward in time, while others can only be made comparing backward in time, the frames of satellite data must be considered sequentially in pairs. For example, frames 1 and 2 are considered together. The CEs in frame 2 are checked to determine if they are overlapped by any CEs in frame 1, then the CEs in frame 1 are checked to determine if they are overlapped by any CEs in frame 2. Then, in a similar manner, frames 2 and 3 are compared both backward and forward, then frames 3 and 4, and so on until the last pair of frames is reached.

If two clusters, each consisting of a series of CEs, merge after several time steps, then all of the CEs belonging to both clusters are assigned the same unique cluster label. All clusters which either start at the first time frame or end at the last, or which touch a boundary of the analysis domain at any time, are not considered in our results.

b. *An example of the algorithm's performance*

We found that the tracking algorithm identified and followed cloud clusters much as one would view pictures subjectively. The performance of the routine can be compared to the results of Churchill and Houze (1984), who used manual identification and tracking techniques. Figure 3 shows cluster elements identified by the tracking algorithm during the sequence of times studied by Churchill and Houze. The temperature threshold used here (243 K) is almost identical to the 244.5 K that they employed, and the labels A, B and C are the same that they used to designate the three cloud features that they studied intensively. (The 243 K threshold is used only for this example; 213 K is used elsewhere in this paper). Features B and C were identified as clusters and tracked by the algorithm just as they were subjectively by Churchill and Houze. According to the algorithm, feature B was a cluster made up of the sequence consisting of CEs 8 and 6 at 0100, CE 4 at 0400, CE 2 at 0700, CE 3 at 1000, CE 9 at 1300 and CE 3 at 1600 LST, and feature C was a cluster consisting of CEs 12 and 14 at 1300, CE 8 at 1600 and CE 13 at 1900 LST. Note that the algorithm captured the mergers of two CEs that occurred in the beginning time periods of both B and C. The very small feature A is an example of a CE that was not identified by the algorithm as a cloud cluster because it did not meet the minimum size criterion at either 1600 or 1900. Even if it had, a match would not have been made, because it had moved too far during the 3 h time interval. (Feature A was of special interest to Churchill and Houze despite its small size because it was penetrated by research aircraft.)

c. *Possible errors*

The possible effects of location errors in the satellite data on the identification and tracking of clusters by the above methods were considered. It is known that the GMS-1 contained errors in location as great as 10

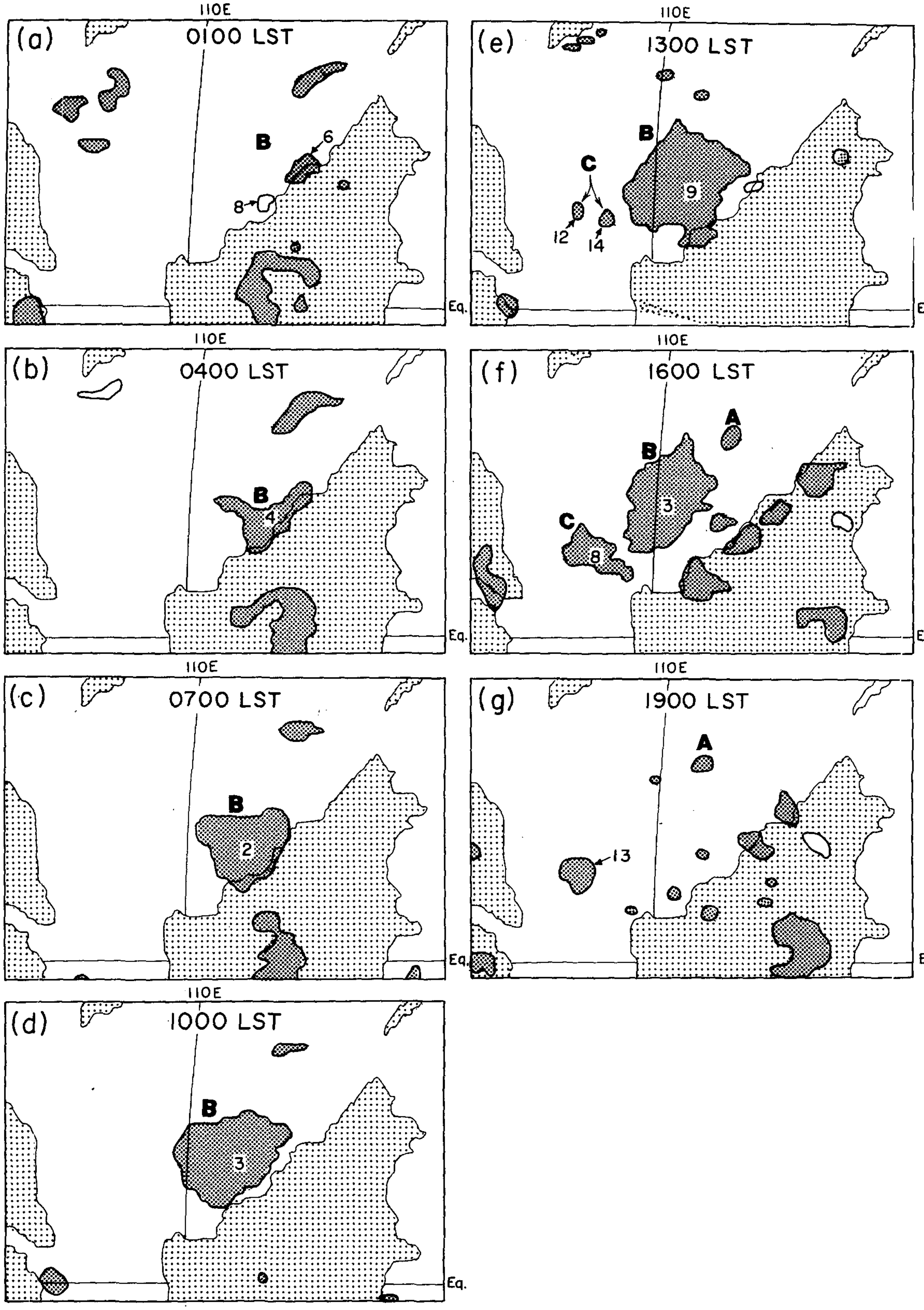

FIG. 3. Sequence of frames of satellite imagery from 11 December 1978. Heavily shaded regions indicate cloud areas with infrared temperature ≤ 30°C. Lighter shading indicates land areas. Cluster elements (CE's) constituting the features A, B and C, which were studied by Churchill and Houze (1984), are indicated by numbers.

or more pixels (Martin and Howland, 1986). An error of 10 pixels is about 2.4 km. A CE of area 5×10^3 km^2 (the smallest considered in this study) has dimensions of about 70 × 70 km, while those 3×10^5 km^2 are 170 × 170 km and those 10^5 km^2 are 320 × 320 km (Fig. 1). From these dimensions, it is evident that there may have been some problems with tracking of very small clusters, but any sequence of CEs with areas reaching 10^4 km^2 or more should have been tracked accurately; at this size the dimensions are considerably larger than the navigation errors and so sufficient overlapping should occur to ensure correct matching.

Another potential error in the matching scheme can result from cloud movement. This error is analogous to that of navigation. A cloud movement of 24 km in 3 h would produce the same error as a 10-pixel navigation error. Rates of movement up to about twice this value occurred in Winter MONEX. Again, there may have been some inaccurate tracking of the very smallest clusters.

An attempt was made at an early stage of the research to modify the matching scheme to account for cluster movement by applying the movement calculated from the first match to the CE before testing for the next match in the sequence. Experience showed that the spurious movements tended to be generated when irregular growth, merges or splits occurred, and the CEs would be moved to an incorrect position. It seemed to us that more reasonable matches were obtained without attempting to correct for cluster motion.

Given the uncertainties of both navigation and cluster motion, it is evident that the tracking routine is fine for medium and large clusters and probably accurate for most smaller ones. However, the technique will certainly contain some errors for very small clusters. These errors are difficult to quantify, but our definite impression is that they are not great enough to affect major conclusions obtained by applying the algorithm.

4. Spatial distribution and temporal variability of cloud cluster characteristics

Five types of information can be extracted from the cloud cluster identification and tracking routine: (a) the area covered by cloud; (b) the frequency of occurrence of cloud at a given location; (c) the location and times of initiation, midlifetime and dissipation of clusters; (d) lifetimes of clusters; and (e) track of clusters. In this section, we examine the spatial and temporal variability of these characteristics as obtained by applying the identification and tracking algorithm to WMONEX cloud clusters.

In the Winter MONEX area, the spatial variability is closely linked to the complex distribution of land and sea characterizing the "maritime continent." The temporal variability is dominated by two factors: The diurnal cycle and the alternation of "surge" and "nonsurge" conditions. Surge conditions refer to periods when the surface northeasterlies become intensified across the South China Sea, in association with synoptic-scale variability of the monsoon flow over Asia at higher latitudes, and cloudiness over the maritime continent (especially northern Borneo) becomes enhanced (Ramage, 1971). In view of these known controls over weather in the maritime continent region, the five types of information [(a)–(e)] just listed are examined here with regard to their (i) spatial distribution among the various land masses and seas, (ii) diurnal time variability and (iii) variation in time with respect to occurrence or nonoccurrence of surge regimes over the area.

a. Area covered by cloud

In section 5, we will examine the statistical distribution of the sizes of clusters and CEs detected by the tracking routine. Here we only examine the gross distinction of the total area covered by cloud over land and sea. Each CE was assigned to land or sea, depending on the location of its area-weighted centroid. The area of each CE was then added to a cumulative cloud area observed in each category for each of the eight observing times. This procedure was repeated for each of the 21 days and then the total cloud amounts over the land and the sea were added for the entire period. The results are shown in Fig. 4.

There is a very strong diurnal signal evident. The cloud cover over the sea reaches a maximum of nearly 4×10^6 km^2 at 1000 and then falls off sharply to a minimum of less than 10^6 km^2 at 1900, after which the cloud cover starts to increase slowly. Examination of individual cloud pictures suggests that this initial increase in cloud cover over the water is largely caused by clusters centered over the land moving to the sea. The strong increase in cloud cover in the early hours of the morning on the other hand is caused by the rapid growth of new cloud clusters forming over the ocean.

The signal over the land is quite the opposite to that over the sea. The minimum total cloud cover over the land is at 1300, slightly later than the maximum over the sea. The maximum over the land is at 1900, which corresponds to the minimum over the sea. The observed times of maximum and minimum cloudiness over the land and the sea correspond very closely to those found by Houze et al. (1981), the only difference being that the observed maximum cloudiness over the land is slightly earlier in this study than theirs.

The lowest graph in Fig. 4 shows the area of cloud cover over land, but not including Borneo. The diurnal signal is similar, but with reduced amplitude, as the area of all land masses except Borneo is quite small.

b. Frequency of occurrence of cluster elements as a function of time and space

In Figs. 5 to 8 the study area is divided into 120 squares of approximately 240 by 240 km, or 5.76

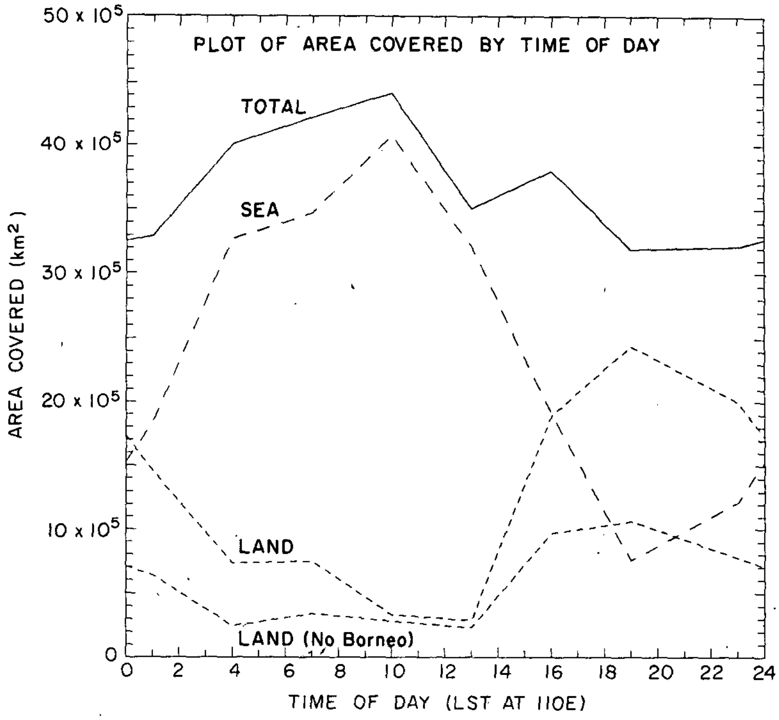

FIG. 4. Time variation of total accumulated cloud cover over land and sea. The total accumulated cloud areas were computed as the sum of the areas of individual CEs. Each CE was assigned to land or sea depending on whether its centroid was over land or sea. The curves show the total cloud over all land, all land except Borneo, the sea, and total cloud cover. The CEs which touched a domain boundary are not included in the totals.

× 10^4 km^2 in area. Whenever the centroid of a CE falls within one of these areal subdivisions then a mark is added to the "box." The total number of marks in each "box" then represents the total number of times a CE centroid was located within this area. Contours of these values are then drawn representing the "number density" of CEs. In Figs. 5 to 7 only CEs with areas $\geqslant 3 \times 10^4$ km^2 are included in the totals (see inset in Fig. 1).

Figure 5 shows that most of the larger CEs were observed over the ocean and that there was a strong preference for the areas off the northwest coast of Borneo, the island of Bangka and over the Java Sea. There was also a tendency for CEs to occur over southern Borneo and Sulawesi. (Locations are identified in Fig. 1.)

The total data set was divided into morning and evening periods, which correspond to the diurnal peaks over sea and land seen in Fig. 4. The morning period includes the observing times 0400, 0700, 1000 and 1300 while the evening period is made up of all the remaining times. The number densities for the morning period (Fig. 6a) were maximum over the ocean, which reaffirms the results shown in Fig. 4. The most obvious center of action was off the northwest coast of Borneo. Houze et al. (1981) and Johnson and Kriete (1982) have previously described this strong morning maximum. Other maxima appeared just north of the island of Bangka and over the Java Sea. The northwest South China Sea, the Strait of Makassar and the Celebes Sea are ocean areas which showed almost no activity. During afternoon (Fig. 6b), fewer CEs were observed and most of these were in the coastal regions of Borneo and the other islands where local sea breeze circulations evidently enhanced cloud cluster growth. By comparing the number 2 contour, which defines the outer boundary of CE number density, between Figs. 6a and 6b, it can be seen that the general area of activity between these two time periods reverses, highlighting the strong diurnal oscillation in the region.

To examine cloud-cluster characteristics in relation to the strength of the monsoon, the data were divided into surge and non-surge periods. A surge period was defined as any time in which the mean wind speed was at least 10 m s^{-1} at the two Soviet observing ships located in the South China Sea at 7°N, 109°E and 7°N, 113°E. The surge days were 11 to 17 December inclusive and 23, 24, 28 and 29 December 1978. The remaining periods were classified as nonsurge. By this definition there were 11 surge days and 10 nonsurge

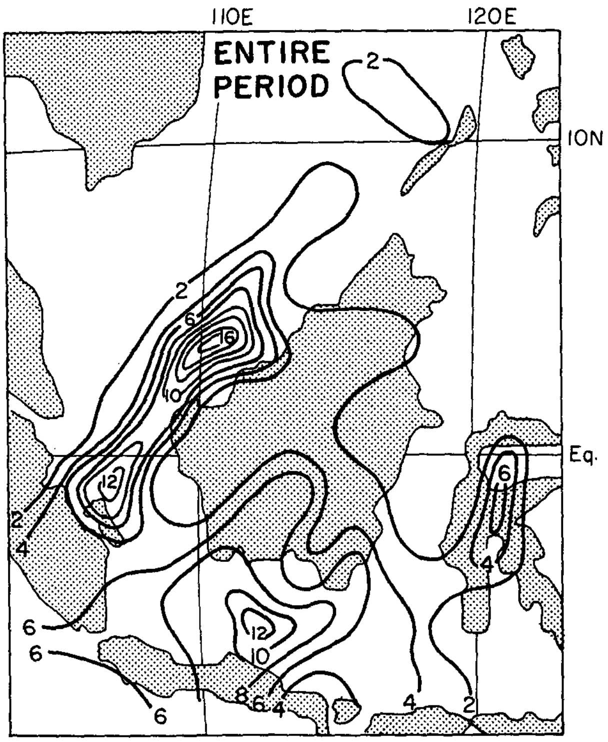

FIG. 5. Frequency of occurrence of CE's with areas of at least 3 × 10^4 km^2. The total area is divided into 120 "boxes," each area approximately 240 by 240 km. The contours represent the total numbers of CE's counted in each box over the entire 21 day observing period.

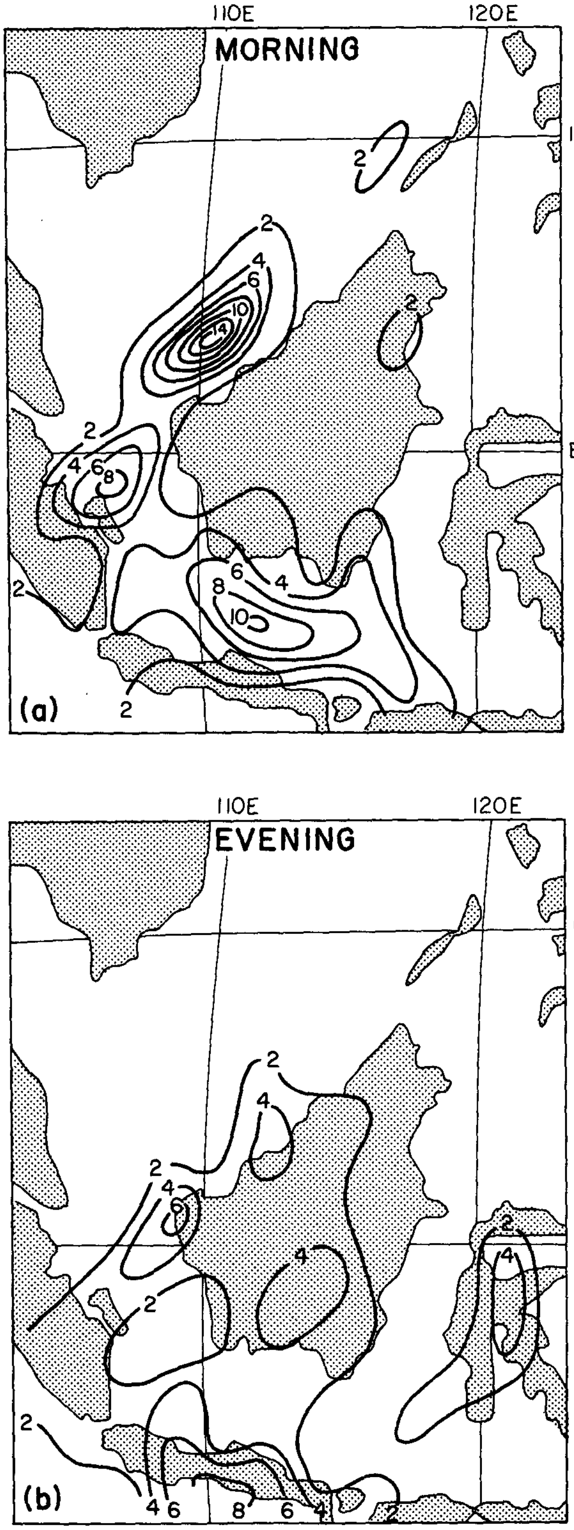

FIG. 6. Diurnally separated number of CEs. The contours are as in Fig. 5. (a) CEs counted during the morning period defined as the observing times of 0400, 0700, 1000 and 1300 LST. (b) The CEs counted during the evening period defined as the observing times 1600, 1900, 2300 and 0100 LST.

days. The totals for the surge period were normalized to 10 days so that contours of the number densities of CEs could be compared directly between surge and nonsurge periods.

Figure 7 shows that during the surge periods, an elongated maximum extended from west of the Philippines, off the northwest coast of Borneo, to the northeast coast of Sumatra. Although the surge conditions may have influenced convection over the Java Sea, it has been shown by Davidson et al. (1983) that a disturbance, probably with Southern Hemisphere influences, moved across the region initiating widespread convection at this time. During the nonsurge periods, the elongated maximum referred to heretofore was reduced to only a localized area of activity off the northwest Borneo coast, where diurnal controls were apparently still generating favorable conditions for genesis of clusters.

c. Comparisons of subtotals for small and large CEs

Figure 8 shows the number density of CEs smaller in area than 3 × 10^4 km^2. Comparing Fig. 8 with Fig. 5, we see that generally the number densities were maximum in much the same areas for both the large

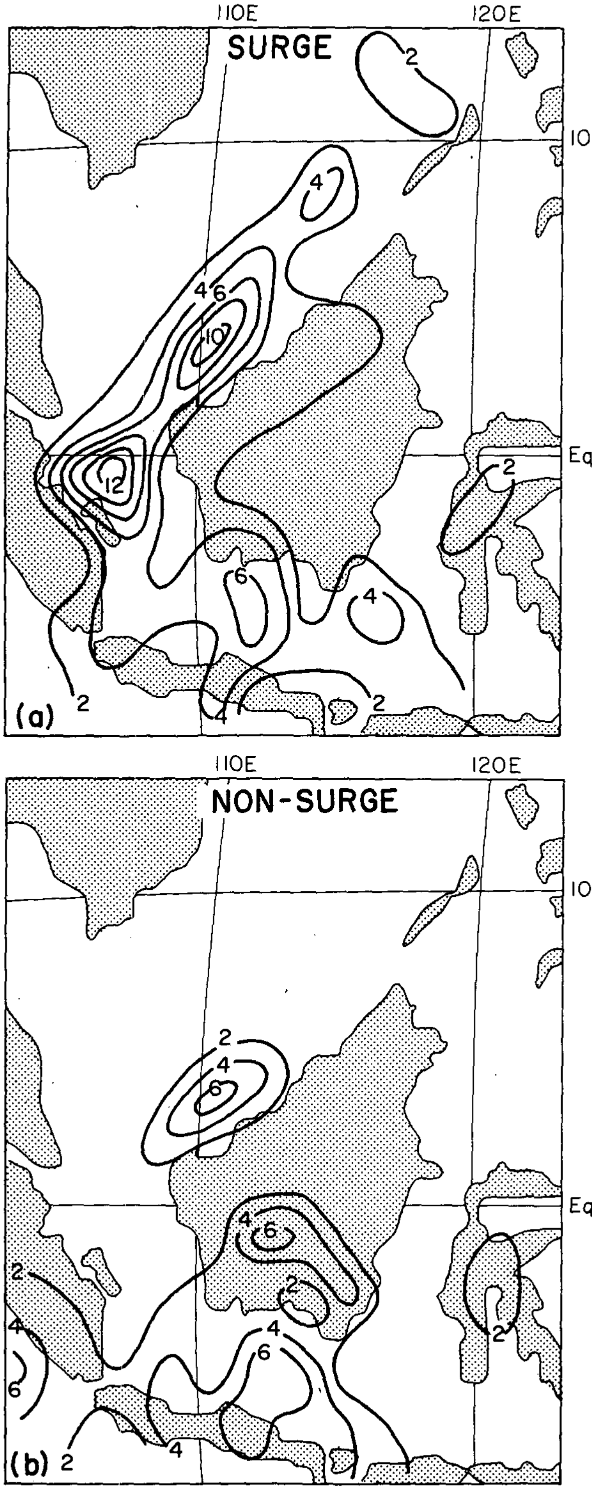

FIG. 7. Number of CEs separated into surge and nonsurge periods. The contours are as in Fig. 5. The surge periods are those days in which the mean wind at the two Soviet observing ships at 7°N 109°E and 7°N 113°E (Fig. 1) was 10 m s^{-1} or greater, and nonsurge periods all other times. The surge periods included 11 to 17 December and 23, 24, 28 and 29 December. The surge period is normalized to 10 days so that the numerical values of the contours are comparable.

and small CEs. This is to be expected as many of the small CEs counted would represent the developing and decaying stages of large cloud clusters. The strait of Makassar, however, contained a large population of small CEs where few large CEs were observed. In this location, large numbers of small clusters developed but did not grow into large mesoscale systems. The physical mechanism restricting the growth of these clusters is not evident.

d. Locations of clusters at initiation, mid-lifetime and dissipation

In Figs. 4–8, we have examined the spatial distributions of CEs, where each CE is defined as an area of cloud at a particular observing time. No account has been taken of the life cycles of clusters which are made up of the time sequences of CEs identified by the tracking routine. The midpoint, which is defined as the area-weighted centroid of the CE or group of CEs, at the beginning of the sequence identifies the initiation point of the cluster, while the midpoint at the last time locates its dissipation point.

The spatial distribution of the midpoints of clusters at initiation, midtime and dissipation time are shown in Figs. 9–11 for clusters with maximum areas of at least 3 × 10^4 km^2 and minimum lifetimes of at least 6 h. The point plotted for each cluster in Figs. 9 and 10

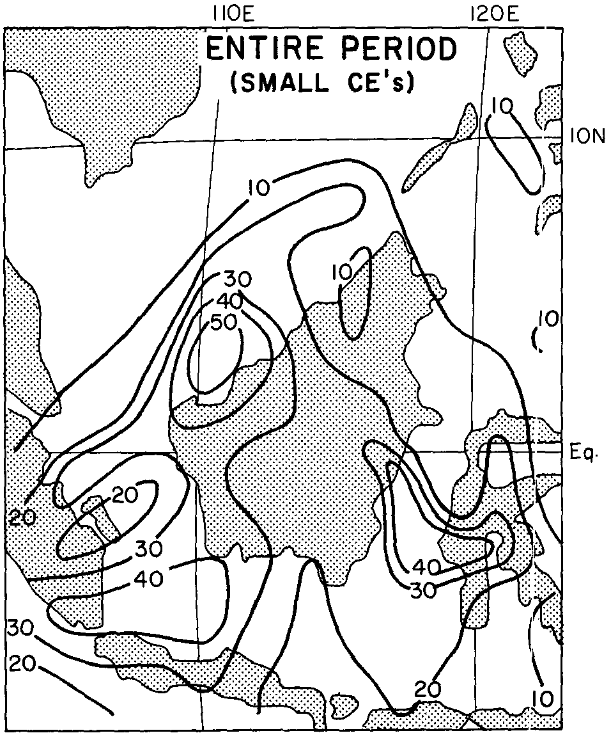

FIG. 8. As in Fig. 5 but for CEs with areas less than 3 × 10^4 km^2.

is designated as occurring during the morning or afternoon period as defined before. In Fig. 11, the points are separated into "day" and "night," rather than morning and evening, where the day period includes the observational times 0700, 1000, 1300 and 1600, while the night period includes the remaining times. These are the two time groups wherein the decay times were best separated between land and sea.

The cluster initiation points were clearly divided between morning and evening (Fig. 9). Clusters which developed over land tended to do so during the evening period, the only exceptions being located near the coast. Conversely, nearly all the clusters which developed over the sea did so during the morning.

The spatial distribution of cluster midpoints at midlifetime approximates the spatial distribution of CE midpoints (cf. Figs. 5 and 10). However, close examination of Fig. 10 reveals that there are few points near the island of Bagka, whereas there is a strong maximum seen in that area in Fig. 5. This comparison indicates that in this area there were a few long lived clusters, comprising many CEs, which were accumulated into the totals seen in Fig. 5. The maxima seen in Fig. 10 over the sea off the northwest coast of Borneo and over the Java Sea were, on the other hand, the result of more numerous individual clusters. The midtimes of clusters over water were during the morning hours with very few exceptions. On the other hand, the midtimes over the land nearly always occurred during the evening.

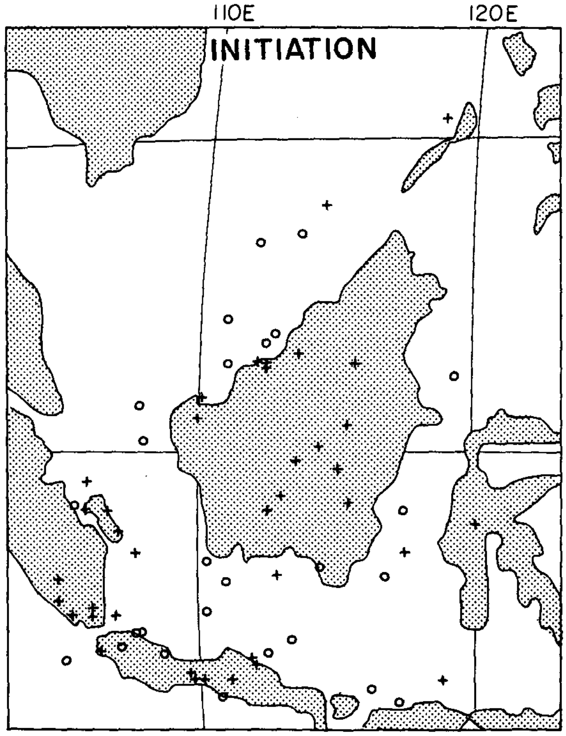

FIG. 9. Midpoints of clusters at initiation for "large" clusters, i.e. those which reached a maximum area of at least 3 × 10^4 km^2 and had a lifetime of at least 6 h. The clusters that had an initiation time of 0400, 0700, 1000 or 1300 are marked with 0 and all other times are marked with +.

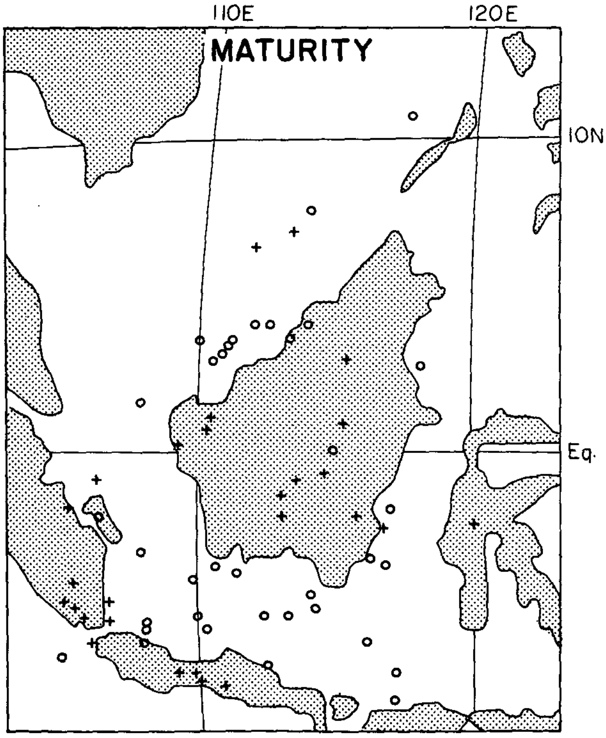

FIG. 10. Midpoints of clusters at midlifetime for large clusters as defined in Fig. 9.

For decaying clusters (Fig. 11), there was not the predominance of locations near the coast that there was at start times, and there were considerably more clusters well out to sea at the end points than at the start points. Also the diurnal signal was very strong. Of those clusters that decayed well out to sea, every one dissipated during the daytime. Likewise for those clusters well over the land, every one dissipated during the night.

e. Tracks and lifetimes of clusters

Figure 12 shows the tracks of all clusters that reached a maximum size of 3 × 10^4 km^2 and had a lifetime of at least 6 h. Each arrow joins the genesis point with the end point, and the number next to each arrow is the lifetime of each cluster in hours. There is very little obvious order to the directions of the arrows. The only area where there appears to have been any preferred direction of motion is off the northwest coast of Borneo where clusters tended to form near the coast and move out to sea. Elsewhere there was only a slight tendency

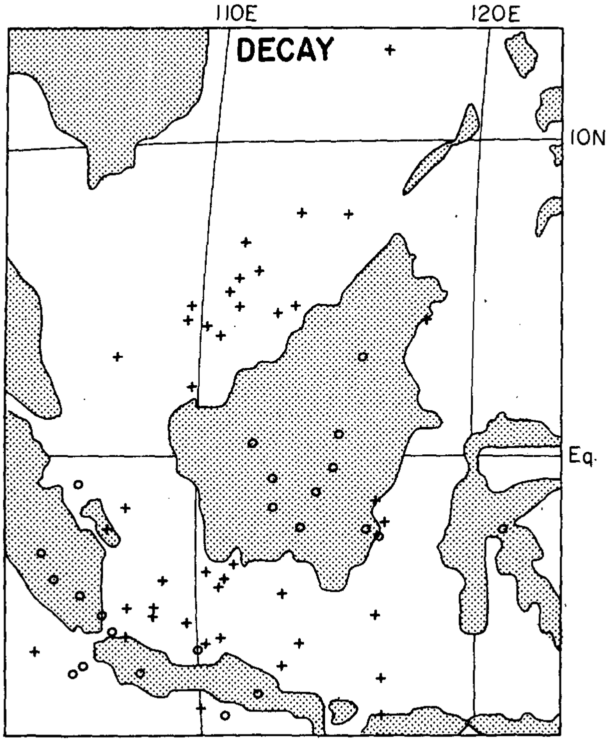

FIG. 11. Midpoints of clusters at time of decay for large clusters are defined in Fig. 9. The clusters that had a dissipation time of 0700, 1000, 1300 or 1600 are marked with 0 and all other times are marked with +.

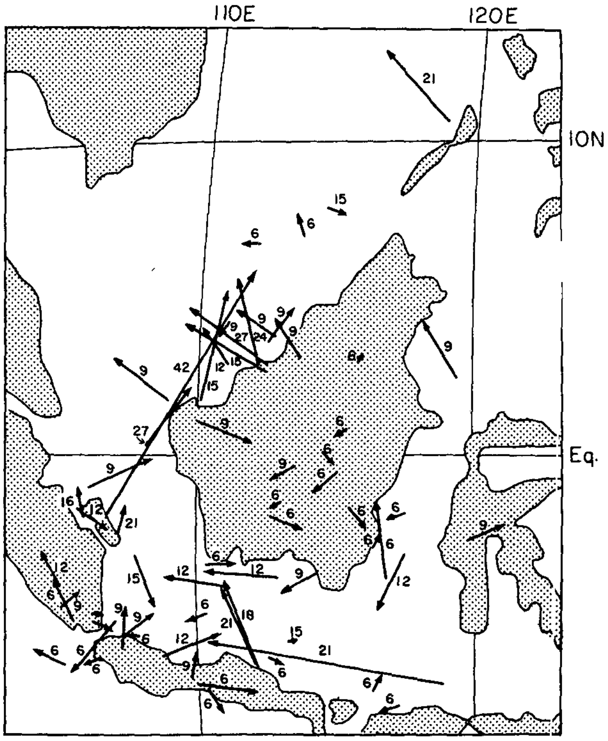

FIG. 12. Movement of all large clusters during the 21-day period of observation. Large clusters are as defined in Fig. 9. Each arrow joins the initiation point with the decay point of a cluster. The arrow heads are at the end points. The numbers alongside each arrow represent the lifetime of the cluster in hours.

for clusters to move from the land to the sea. The cluster lifetimes indicated in Fig. 12 show that clusters which resided over the land tended to have shorter lifetimes than those over the sea.

5. Cloud cluster size spectrum

In this section, the size variations of cloud clusters and their elements, as detected by our objective method, are examined three ways. First, the numbers of CEs in various size categories are considered. Then, these numbers are weighted by the area covered by the CEs in each size category. Finally, the results of the tracking routine, which groups CEs into time-sequences comprising individual cloud clusters, are used to determine how clusters that attained various maximum sizes contributed to the total WMONEX cloud cover.

a. Number distribution of cluster element size

The number of CEs of various sizes that occurred over the 21 day period of WMONEX are indicated in Fig. 13. The bars of the histogram indicate the contribution of CEs in a given size range to the total number of CEs observed. This total is given by

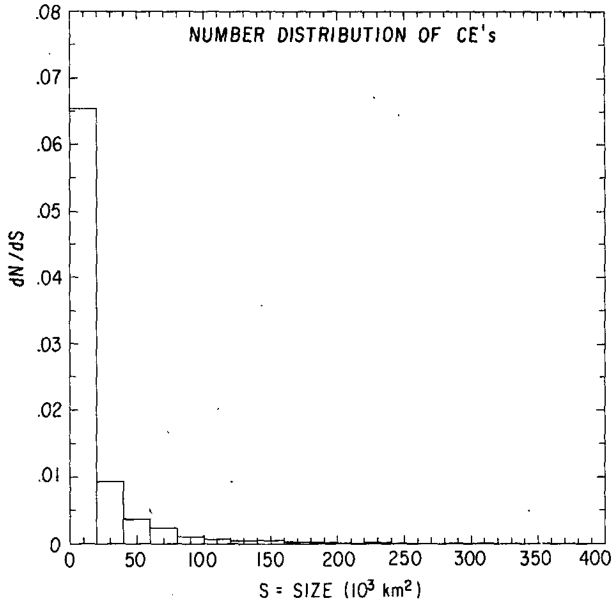

FIG. 13. Number distribution of CEs for the full 21 day period. Here S is the size of a CE in km^2; dN/dS is the number of CEs in a size category per increment of size.

$$N_T = \sum_i N_i = \sum_i (dN/dS)_i \Delta S = \int_0^\infty (dN/dS)dS, \quad (1)$$

where S is the CE size (in units of area), N_i the number of CEs in a size interval S_i to $S_i + \Delta S$, and the summation is over all size intervals. The quantity (dN/dS) is the size distribution function for N_T, and $(dN/dS)_i$ is the value of the size distribution function in a particular size interval. From (1), it can be seen that the total number of CEs (N_T) is given by the integral of (dN/dS) over all S (i.e. the total area under the curve in Fig. 13) and that the contribution of the CEs in a given size interval to this total is N_i, which is the area of one bar of the histogram $[(dN/dS)_i \Delta S]$.

It is clear from Fig. 13 that most CEs fall within the smaller size groups. In fact, 83% of the CEs were in the smallest size group ($<2 \times 10^4$ km^2), while 91% of all CEs were less than 4×10^4 km^2 in area. The very large CEs only accounted for a very small proportion of the total number of CEs; this fact is illustrated by the second column of Table 1, which indicates the cumulative number of CEs exceeding various sizes.

Figure 14 shows the plot of CE area on a logarithmic scale against the cumulative frequency on a probability scale. The O's represent the cumulative frequencies of the CEs observed over the land and the X's those over the sea. The straight line represents the lognormal distribution computed from a hypothetical size distribution s^*. The logarithms of s^* have a mean of 3.56 km^2 and a standard deviation of 0.78 km^2. The mean of the logarithms of s^* transforms to a mean of s^* of 3.63×10^3 km^2. López (1976, 1977, 1978) and Houze and Cheng (1977) have used this type of presentation to show that radar echoes from tropical precipitation are distributed lognormally.

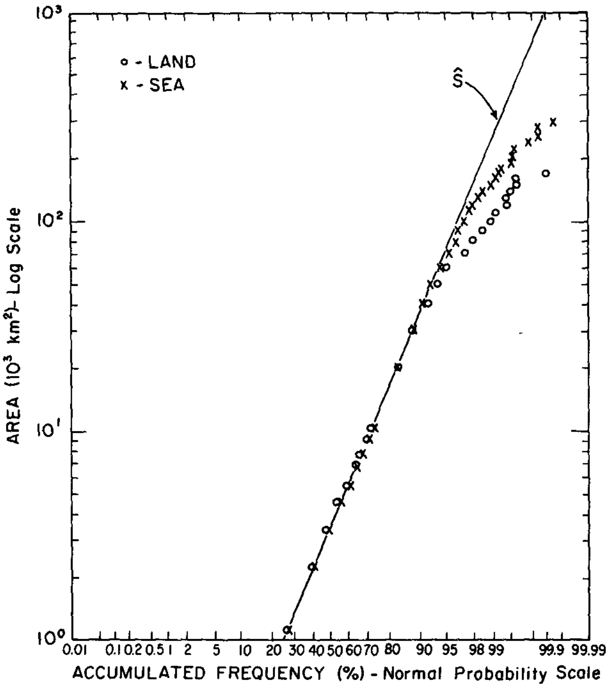

FIG. 14. Accumulated frequency distribution of CE areas for the full 21 day period. The O's represent the number of CEs over the land while the X's represent the number of CEs over the sea. The solid line is the lognormal distribution of a hypothetical size distribution s^*.

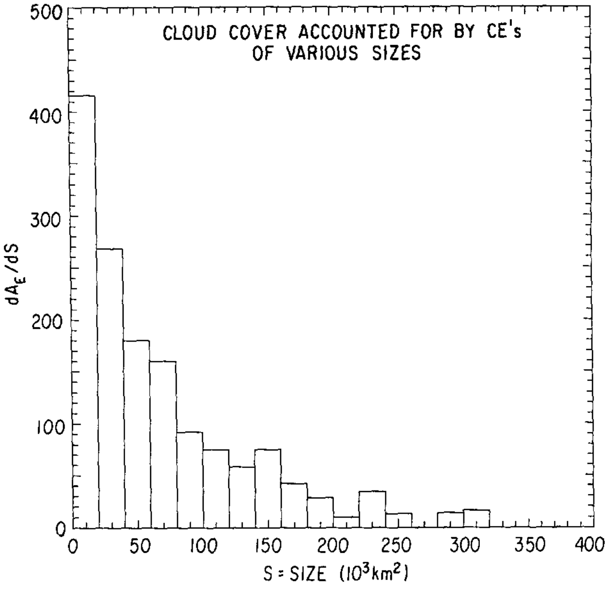

FIG. 15. Areal cloud cover accounted for by CEs of various sizes. Data from full 21 day period are included. Here S is the size of a CE in km^2; dA_E/dS is total area covered by cloud per increment of CE size.

Application of the chi-square test of goodness of fit to the straight line for both land and sea for CEs of area 6×10^4 km^2 or less yielded values of χ^2 of 3.2 for the land and 7.8 for the sea with 9 degrees of freedom. Neither value is significant at the 1% level, and so the hypothesis that both size distributions for clouds sizes less than 6×10^4 km^2 belonged to the hypothetical lognormal distribution cannot be rejected. However Fig. 14 shows that CEs with sizes greater than 6×10^4 km^2 over land and 1.2×10^5 km^2 over sea departed from the lognormal distribution; i.e., both the observed distributions behaved as truncated lognormal distributions (López, 1977). In fact, no CE sizes greater than 1.6×10^5 km^2 were observed over the land, and no CE sizes greater than 3.0×10^5 km^2 were observed over the sea. These results suggest that the mechanisms which led to the development and growth of cloud clusters over land and sea were the same, but that same physical process limited the growth of clusters over land for sizes in excess of 6×10^4 km^2, and over the sea for sizes greater than 1.2×10^5 km^2. Although the truncation occurs for only the largest 5% of CEs, it will be

TABLE 1. Accumulated number of and area covered by CEs exceeding various sizes.

Size ($\times 10^4$ km^2)	Total number of CEs (%)	Total area covered by CEs (%)
1	27	83
2	17	72
3	12	62
4	9	54
6	5	42
10	2	25

shown shortly that these few large CEs account for a large percentage of the total cloud cover.

b. Areal distribution of cluster element size

The number distribution dN/dS examined in subsection 5a de-emphasizes the importance of the large-scale categories since it gives as much weight to a small CE as it does a large one. It is therefore useful to consider how the total area covered by cloud is accounted for by various sizes of CE. We let A_{ET} represent the total area covered by all the CEs of all sizes that occurred during the 21 day period of study. Then

$$A_{ET} = \sum_i A_{Ei} = \sum_i (dA_E/dS)_i \Delta S = \int_0^\infty (dA_E/dS)dS, \quad (2)$$

where A_{Ei} is the combined area covered by all the CEs whose sizes fell in the interval S_i to $S_i + \Delta S$, and the summation is over all size intervals. The quantity (dA_E/dS) is the size distribution function for A_{ET}, and $(dA_E/dS)_i$ is the value of the size distribution function in the size interval S_i to $S_i + \Delta S$. From (2), it can be seen that the total area covered by all CEs (A_{ET}) is given by the integral of (dA_E/dS) over all S. This integral is the total area under the histogram shown in Fig. 15. The contribution to the integral by the CEs in a given size interval $[(A_E)_i]$ is the area of one bar of the histogram $[(dA_E/dS)_i \Delta S]$.

By comparing Figs. 13 and 15 it can be seen that a few CEs in the larger size groups accounted for a large proportion of the total cloud cover. Table 1 compares the accumulated percentage of numbers of CEs with their accumulated percentage areas. For example, CEs with areas greater than 2×10^4 km^2 accounted for only 17% of the total number of CEs but 72% of the total area covered by CEs. The CEs over 10^5 km^2 in area, which account for only 2% of the CE numbers, account for fully 25% of the total areal coverage.

Differences between land and sea are indicated by Figs. 16a and b. In particular, the truncation over the land just described is apparent in Fig. 16; for example, CEs with an area of greater than 10^5 km^2 account for only 12% of the cloud area over land but 31% of the total area over the sea.

c. Areal distribution according to maximum size attained

The tracking routine can be used to great advantage to construct an areal distribution defined rather differently than that just described. In section 3, a cloud cluster was defined as a sequence of CEs that can be tracked from one frame of images of the next. The cumulative area covered by a cloud cluster throughout its lifetime can then be defined as

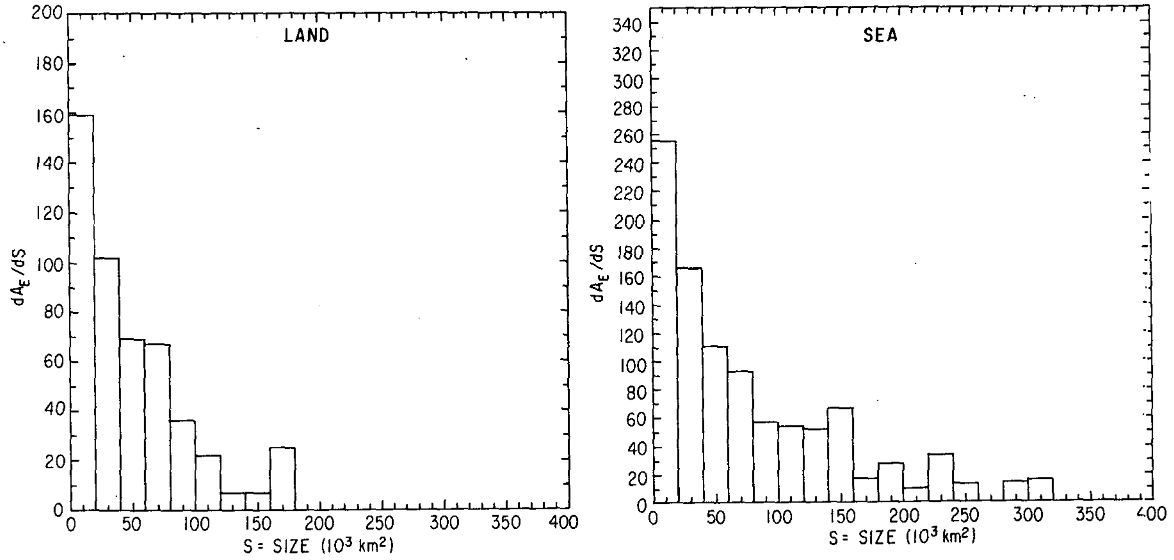

FIG. 16. As in Fig. 15 except data have been separated according to whether the CEs were centered over land or sea.

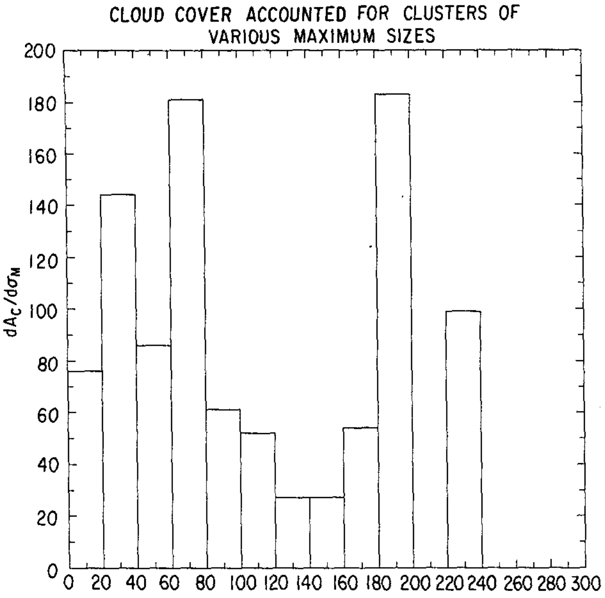

FIG. 17. Areal cloud cover accounted for by clusters of various maximum sizes. Data from the full 21 day period are included. Here σ_M is the maximum size attained by a cluster in its lifetime; $(dA_C/d\sigma_M)d\sigma_M$ is the total area covered by all clusters that had maximum sizes in a size range of width $d\sigma_M$. See text for further explanation.

$$\sigma_T = \sigma(t_1) + \sigma(t_2) + \cdots + \sigma(t_f), \tag{3}$$

where $\sigma(t_i)$ is the area covered by the cluster in the frame corresponding to time t_i, and t_f is the time of the final frame in which the cluster appears. The maximum size attained by the cluster during its lifetime is

$$\sigma_M = \text{maximum}(\sigma_i), \quad i = 1, \cdots, f. \tag{4}$$

The quantity A_{Ck} is defined as the sum of the σ_T's of all the clusters whose maximum sizes fall in the interval σ_{Mk} to $\sigma_{Mk} + \Delta\sigma_M$. Then, the total area covered by all cloud clusters is given by

$$A_{CT} = \sum_k A_{Ck} = \sum_k (dA_C/d\sigma_M)_k \Delta\sigma_M$$
$$= \int_0^\infty (dA_C/d\sigma_M)d\sigma_M, \tag{5}$$

where the quantity $(dA_C/d\sigma_M)$ is the size distribution function for A_{CT}, $(dA_C/d\sigma_M)_k$ is the value of the size distribution function in the size interval σ_{Mk} to $\sigma_{Mk} + \Delta\sigma_M$, and the summation is over all size intervals. From (5), it also can be seen that the total area covered by all of the identified cloud clusters (A_{CT}) is given by the integral of $(dA_C/d\sigma_M)$ over all σ_M (i.e., the total area under the curve in Fig. 17) and that the contribution of the clusters in a given interval of maximum size to this total (A_{Ck}) is the area of one bar of the histogram $[(dA_C/d\sigma_M)_k\Delta\sigma_M]$.

The total areas under the curves in Figs. 15 and 17 (A_{ET} and A_{CT}, respectively) should be identical, as they both represent the total area of cloud cover during the period of study, were it not for two sampling problems:

1) Some small CEs were not matched with CEs in adjacent time frames, either because they were transitory or moved too far during the 3 h time period between frames to be matched. This resulted in those CEs being added to the CE totals but not the cloud-cluster totals.

2) Clusters which at any time intersected a boundary were not included in the area totals. Many of the CEs which formed the components of such clusters did not touch a boundary and so the area under the curve in Fig. 17 is considerably less than the area under the curve in Fig. 15. Unfortunately, this constraint imposes a bias against large long-lived clusters as they had the highest probability of intersecting a boundary at some time of their lives.

Figures 15 and 17 are very different. Figure 17 and Table 2 both show that most of the area of cold cloud top in WMONEX was accounted for by the clusters which attained the largest maximum sizes. For example, clusters with maximum areas of greater than 2 × 10^4 km^2 accounted for fully 92% of the accumulated cloud cover. Clusters with maximum area greater than 4 × 10^4 km^2 accounted for 77% of the total cloud cover, and the very few clusters which reached a maximum size of 10^5 km^2 account for 45% of the accumulated area. Since about 200 clusters were tracked, these percentages should be fairly representative of the wintertime cloud population over the maritime continent.

It is well known that the area covered by cold cloud top is related (roughly) to precipitation, which is in turn related to latent heat release. Figure 17 can therefore be regarded as an indicator of how the latent heat released over the maritime continent during Winter MONEX was distributed among cloud clusters of different maximum size. The implication is that most of the heating in this region was the result of cloud clusters which reached large maximum sizes.

To ascertain the difference in areal distributions of clusters over land and sea, the clusters were divided

TABLE 2. Portion of total WMONEX cloud cover accounted for by clusters that attained various maximum sizes.

Maximum size attained by cluster (×10^4 km^2)	Total cloud cover accounted for (%)
1	98
2	92
3	86
4	77
6	69
10	45

into two groups: one in which the cluster's midpoint was located over the land during two-thirds of the total cluster lifetime, and another in which the cluster's midpoint was located over the sea during two-thirds of the total cluster lifetime. As can be seen from Fig. 18, there is much more cumulative cloud accounted for by the large maximum size groups over the sea than over land. The distribution appears to be bimodal over the sea but not over the land. This demonstrates that the few clusters which attained a large maximum size over the sea accounted for a large proportion of the cumulative cloud area. Over the land, however, since there were few large clusters observed, the cumulative cloud totals were dominated by clusters with smaller maximum size.

Figure 18 suggests that over the land most of the tropospheric heating in WMONEX resulted from clusters which reached a maximum size of about 6 $\times 10^4$ km^2, while over the sea a bimodal distribution prevailed, with the latent heat release divided between a group of smaller clusters, similar to those over the land, and an additional group of gigantic clusters, averaging (1.5–2.0) $\times 10^5$ km^2 in area.

6. Conclusions

Considerable insight into the nature of cloud systems over the WMONEX area has been gained from the study of some 200 cloud clusters. Our technique, which automatically tracks clusters throughout their lifetimes, including growth periods, splits, mergers and decay, reveals detail on the nature of cloud populations and how they are distributed in time and space. Until this study, the numbers, sizes, lifetimes, tracks and diurnal cycles of individual clusters in WMONEX has not been fully documented. No technique other than one which identifies and tracks clusters would have been capable of producing the results we have obtained. The success of our technique in studying WMONEX cloud clusters indicates that it would be quite useful in obtaining cloud-cluster climatologies for other areas and ultimately for the whole tropics.

An important result of our WMONEX survey is that by far most of the cumulative cloud, and hence the total rainfall, was attributable to a few clusters which reached a large maximum size. More than 85% of the cumulative cloud cover was associated with clusters which had a maximum size of 3 $\times 10^4$ km^2 or more. This strongly suggests that a very high percentage of the rainfall in the region came from clusters which belonged to the larger size categories. This being the case, the net diabatic heating in the WMONEX region was likely concentrated at upper levels since the larger clusters probably had large stratiform components and hence heating profiles like those described by Houze (1982) and Hartmann et al. (1984).

The difference in the size distributions of large cloud clusters between land and sea was considerable. Over the sea a substantial proportion of the cloud cover, and hence the rainfall, came from clusters with maximum areas greater than 1.2 $\times 10^5$ km^2, whereas there were no clusters observed in this size category at all over the land. The possibility that more rainfall came from larger clusters over the sea than over land indicates that net diabatic heating profiles may have been different over the sea than over the land.

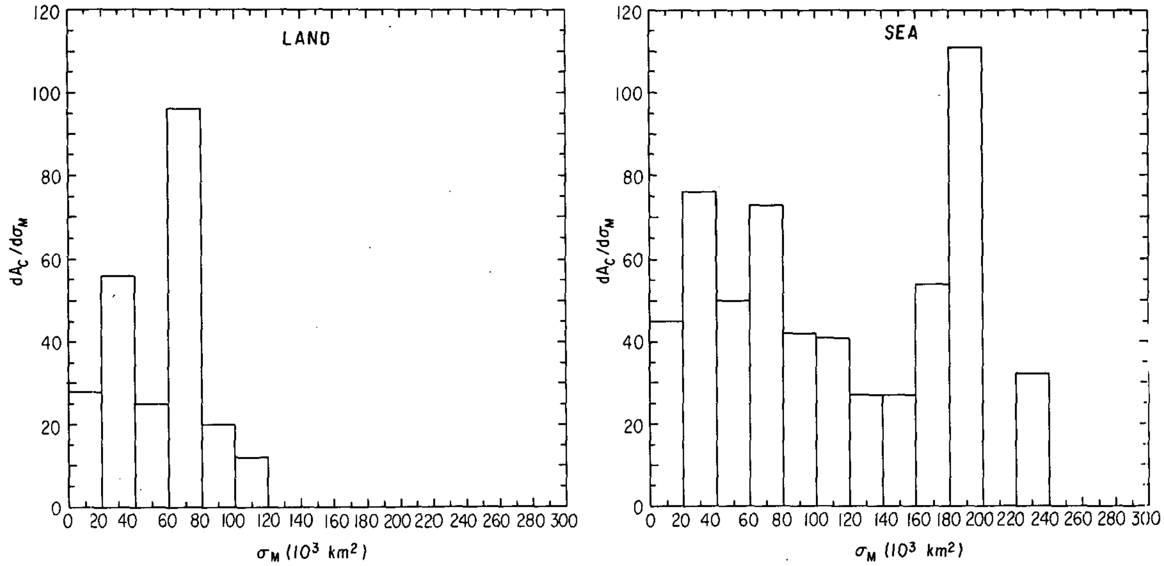

FIG. 18. As in Fig. 17 except data have been divided according to whether the clusters were centered over land or sea at midlifetime.

The size spectra of CEs (i.e., the typical instantaneous cloud-size distribution) over land and water were approximately lognormal, up to a size of about 6 $\times 10^4$ km^2; however, above that size the distribution over the land departed strongly from lognormal, whereas the distribution over the sea followed the lognormal up to size categories of 12 $\times 10^4$ km^2, after which the distribution also showed truncation.

Maps of the geographical distribution of CEs indicate that the occurrence of large CEs (greater than 3 $\times 10^4$ km^2) over the South China Sea was strongly related to the existence or nonexistence of monsoon surges. Synoptic influences thus apparently played a vital role in determining the development of the large clusters. Johnson and Priegnitz (1981) showed that mean high cloud coverage was related to the low- and upper-level divergence fields and that enhanced low-level convergence and upper-level divergence was observed for surge periods. Evidently, large cloud cluster development was associated with enhanced low-level convergence and high-level divergence.

When CE areas over land and sea are totaled, a diurnal signal is strongly evident. This not only supports previous findings (Houze et al., 1981; Johnson and Priegnitz, 1981) but demonstrates the sheer magnitude of this diurnal signal. The cloud area totals over land and sea varied by a ratio of 5 to 1 between day and night. The spatial analyses of both clusters and CEs clearly showed the diurnal signal. Large clusters tended to develop over the land during the evening period and over the sea during the morning period and decay over the sea during the daytime and over the land during the night.

Acknowledgment. This research was supported by the National Science Foundation under Grants ATM80-17327 and ATM84-13546.

REFERENCES

Aspliden, C. L., Y. Tourre and J. B. Sabine, 1976: Some Climatological Aspects of West African Disturbance Lines During GATE. *Mon. Wea. Rev.*, **104**, 1029–1035.

Davidson, N. E., J. L. McBride and B. J. McAvaney, 1983: The Onset of the Australian Monsoon During Winter MONEX: Synoptic Aspects. *Mon. Wea. Rev.*, **111**, 496–516.

Geotis, S. G., and R. A. Houze, Jr., 1985: Rain Amounts Near and Over North Borneo During Winter MONEX. *Mon. Wea. Rev.*, **113**, 1824–1828.

Hartmann, D. L., H. H. Hendon and R. A. Houze, Jr., 1984: Some Implications of the Mesoscale Circulations in Tropical Cloud Clusters for Large-Scale Dynamics and Climate. *J. Atmos. Sci.*, **41**, 113–121.

Houze, R. A., Jr., 1982: Cloud Clusters and Large-Scale Vertical Motions in the Tropics. *J. Meteor. Soc. Japan*, **60**, 396–410.

——, and C. P. Cheng, 1977: Radar Characteristics of Tropical Convection Observed During GATE: Mean Properties and Trends Over the Summer Season. *Mon. Wea. Rev.*, **105**, 964–980.

——, S. G. Geotis, F. K. Marks, Jr. and A. K. West, 1981: Winter Monsoon Convection in the Vicinity of North Borneo. Part 1: Structure and Time Variation of the Clouds and Precipitation. *Mon. Wea. Rev.*, **109**, 1595–1614.

Johnson, R. H., and D. L. Priegnitz, 1981: Winter Monsoon Convection in the Vicinity of North Borneo. Part 1: Effects on Large-Scale Fields. *Mon. Wea. Rev.*, **109**, 1615–1628.

——, and D. C. Kriete, 1982: Thermodynamics and Circulation Characteristics of Winter Monsoon Tropical Mesoscale Convection. *Mon. Wea. Rev.*, **110**, 1898–1911.

López, R. E., 1976: Radar Characteristics of the Cloud Populations of Tropical Disturbances in the Northwest Atlantic. *Mon. Wea. Rev.*, **104**, 268–283.

——, 1977: The lognormal Distribution and Cumulus Cloud Populations. *Mon. Wea. Rev.*, **105**, 865–872.

——, 1978: Internal Structure and Development Processes of C-Scale Aggregates of Cumulus Clouds. *Mon. Wea. Rev.*, **106**, 1488–1494.

Martin, D. W., and A. J. Schreiner, 1981: Characteristics of West African and East Atlantic Cloud Clusters: A Survey from GATE. *Mon. Wea. Rev.*, **109**, 1671–1688.

——, and M. R. Howland, 1986: Grid history: A geostationary satellite technique for estimating daily rainfall in the tropics. *J. Climate Appl. Meteor.*, **25**, 184–195.

Payne, S. W., and M. M. McGarry, 1977: The Relationship of Satellite Infrared Convective Activity to Easterly Waves Over West Africa and the Adjacent Ocean During Phase III of GATE. *Mon. Wea. Rev.*, **105**, 413–420.

Ramage, C. S., 1971: *Monsoon Meteorology.* Academic Press, 157–161.

Webster, P. J., and G. L. Stephens, 1980: Tropical Upper-Tropospheric Extended Clouds: Inferences from Winter MONEX. *J. Atmos. Sci.*, **37**, 1521–1541.

Woodley, W. L., C. G. Griffith, J. S. Griffin and S. C. Stromatt, 1980: The Inference of GATE Convective Rainfall from SMS-1 Imagery. *J. Appl. Meteor.*, **19**, 388–408.